Journal of Alloys and Compounds 622 (2015) 446–457

Contents lists available at ScienceDirect

Journal of Alloys and Compounds

journal homepage: www.elsevier.com/locate/jalcom

Influence of discharge power on the structural, electro-optical, and mechanical properties of (TiZrHf)N coatings

Du-Cheng Tsai [a], Zue-Chin Chang [b], Bing-Hau Kuo [a], Chia-Tai Tsao [a], Erh-Chiang Chen [a], Fuh-Sheng Shieu [a,*]

[a] Department of Materials Science and Engineering, National Chung Hsing University, Taichung 40227, Taiwan
[b] Department of Mechanical Engineering, National Chin-Yi University of Technology, Taichung 411, Taiwan

ARTICLE INFO

Article history:
Received 22 August 2014
Received in revised form 3 October 2014
Accepted 13 October 2014
Available online 19 October 2014

Keywords:
Coating materials
Nitride materials
Vapor deposition
Crystal structure
Transmission electron microscopy
TEM

ABSTRACT

This study aimed to investigate the effects of discharge power on the composition and the microstructural, mechanical, and electro-optical properties of (TiZrHf)N coatings. The coatings were deposited on Si substrates via reactive magnetron sputtering. The coatings were deposited at varying discharge powers (50–300 W). At low discharge powers, amorphous structures were produced during the initial sputtering period. High (200)-axis orientation structures were formed when sputtering time was increased. The upper part of the coatings was composed of open columnar structures with extended voids along the column boundaries. Increasing the discharge power decreased the thickness of the amorphous layer. Consequently, the microstructures became dense and compact; however, the grain size did not change significantly. Meanwhile, an enhanced compressive stress was observed, followed by an increase in the texture coefficients of the (111) plane and lattice parameters. The physical properties of the coatings were improved by increasing the discharge power. The coating hardness was increased to approximately 32.1 GPa. In addition, the electrical resistivity was decreased to approximately 134 μΩ cm, and the light reflectivity in the infrared region (700–2400 nm) was increased to 75%.

1. Introduction

Surface coatings are used in various industries to enhance the mechanical properties and corrosion resistance of substrate materials applied in aggressive environments. Transition metal nitrides are known for their remarkable physical properties, including high hardness and mechanical strength, chemical inertness, and electrical resistivity (i.e., metallic to semiconducting) [1]. As a result, such nitrides have become important in several applications, such as hard wear-resistant coatings, diffusion barriers, and optical thin films. Among the large family of transition metal nitrides, TiN, ZrN, and HfN coatings have received considerable attention because of their outstanding mechanical properties, low resistivity, and distinctive gold color as a result of interband transitions combined with a high reflectance in the red and infrared regions. However, owing to the requirement of better performances, ternary nitrides, which include TiAlN [2], TiZrN [3], and CrZrN [4], have been developed intensively. Compared with conventional binary metal nitrides, ternary nitrides exhibit great advantages in mechanical and oxidation resistance due to their respective alloying effects. In addition, because combined attributes of individual components of the coatings provide high solid solution-strengthening effect; thus, multi-elemental coatings, such as TiAlCrN [5] and TiZrAlN [6], have been developed. Among the promising alternatives of conventional protective coating materials, (TiZrHf)N coating is a challenging substance. (TiZrHf)N nitride coatings are expected to provide superior mechanical property and thermal stability. Moreover, (TiZrHf)N coatings exhibit a distinctive gold color that can be used for decorative purposes.

In this study, a novel (TiZrHf)N coating was synthesized from a set of TiZrHf inset targets via reactive magnetron sputtering. Reactive magnetron sputtering involves different parameters that play important roles in the quality of deposited thin films. However, few studies have been performed to elucidate the effect of discharge power. In addition, the structural evolution of the deposited thin films should be analyzed using scanning electron microscopy (SEM) and transmission electron microscopy (TEM). Only few studies have investigated the electro-optical properties of coatings. Therefore, the present study aimed to investigate the influence of sputtering power on crystal structures and microstructures, as well as the mechanical, electrical, and optical properties of deposited (TiZrHf)N coatings.

* Corresponding author. Tel.: +886 4 2284 0500; fax: +886 4 2285 7017.
E-mail address: fsshieu@dragon.nchu.edu.tw (F.-S. Shieu).

http://dx.doi.org/10.1016/j.jallcom.2014.10.073
0925-8388/

2. Experimental

(TiZrHf)N coatings were deposited on p-Si (1 0 0) wafers using an RF magnetron sputtering system with equimolar TiZrHf targets (75 mm in diameter). The chamber could be evacuated to a base pressure of 1×10^{-6} using a turbomolecular pump along with a rotary pump. The Si substrates were cleaned in an ultrasonic bath with acetone, ethanol, and deionized water at room temperature for 15 min, and then rinsed using deionized water. After rinsing, the substrates were then dried under a stream of nitrogen immediately prior to deposition. The (TiZrHf)N coatings were deposited at a substrate temperature of 723 K in an Ar and N_2 atmosphere and a working pressure of 2.5×10^{-3} Torr. Ar and N_2 flows were maintained at 45 and 5 sccm, respectively. Substrate external bias was not used during deposition. The sputtering power was chosen as the controlling parameter, which was varied from 50 W to 300 W. Deposition time decreased with increased discharge power to maintain the coating thickness at approximately 500 nm. Targets were pre-sputtered with Ar to remove their surface oxide layers before deposition.

Chemical compositions of the coatings were determined by field emission–electron probe microanalyses (FE-EPMA, JOEL JXA-8800M). At least three tests were performed for each sample. Crystal structures were analyzed by glancing-incidence (1°) X-ray diffraction (GIXRD, BRUKER D8 Discover) using Cu Kα radiation at 1°/min scanning speed. The residual stress of the deposited coatings was obtained by acquiring GIXRD patterns at various tilting angles ψ, or acquiring offset scans and plotting the d-space values versus $\cos 2\alpha \sin 2\psi$ technique, where $\alpha = \theta - \omega$ [7]. Morphological studies and thickness measurements were performed using field-emission SEM (JEOL JSM-6700F). The deposition rate was obtained by dividing the thickness of the coating with deposition time. The microstructures were investigated by analytical TEM (JEOL JEM-2100F). Surface roughness (root-mean-square) values of the coatings were acquired using an atomic force microscope (AFM, Seiko SPA400). Microhardness and elastic modulus of the coatings were measured using a TriboLab nanoindenter (Hysitron). At least five measurements were performed for each sample. Electrical resistivity of the coatings was measured using a four-point probe system. Reflectivity was measured using a spectrophotometer (Shimadzu UV-3600).

3. Results and discussion

3.1. Chemical composition and deposition rate

Fig. 1a presents the deposition rates of (TiZrHf)N as a function of discharge power. The deposition rate increased linearly from 0.98 nm/min to 12.44 nm/min when discharge power increased from 50 W to 300 W. The variations in target voltage caused by discharge power are shown in Fig. 1b, in which voltage increases with the increase in discharge power. This direct relationship to the determinacy of deposition rate on the flow of ionized particles (J_{ion}) and its average kinetic energy (KE_{av}) upon striking the target are supported by the Langmuir–Child relationship [8] and the average kinetic energy equation [9] in glow discharge.

$$J_{ion} \propto Voltage^{3/2} \quad (1)$$

$$KE_{av} \propto Voltage \quad (2)$$

The flow of ionized particles generally results in substantial ion bombardment on the target. The high kinetic energy of these ions increased the probability of target atoms to be ejected because of the impact of incident ions. Therefore, both mechanisms contributed to the increased sputter deposition rate.

The content of all of the elements in the (TiZrHf)N coatings deposited under different discharge powers are shown in Fig. 2. Basically, the contents of all metal elements in both films remained at constant values with different discharge power. Noticeably, the low discharge powers (⩽100 W) resulted in higher O_2 content and lower N_2 content, which were due to the low deposition rate. The O_2 source in the coating is yet to be identified; however, the following sources were suggested: the residual gas and plasma or heating-induced desorption from the deposition chamber. The difference between the electronegativity of oxygen (3.44 eV) and that of the target element was higher compared with that of N_2 (3.04 eV). Thus, at very low deposition rates, the O_2 was incorporated in the growing coating more readily [10]. At low discharge powers (50 and 100 W), the coatings contained significant O_2 content, therefore, in this case we have (TiZrHf)ON coating instead of (TiZrHf)N coating. However, beyond this discharge power of 100 W, the O_2 content became nearly constant. This could be attributed to the increased ionization probability of oxygen at higher discharge powers [11]. The almost unchanged O_2 content

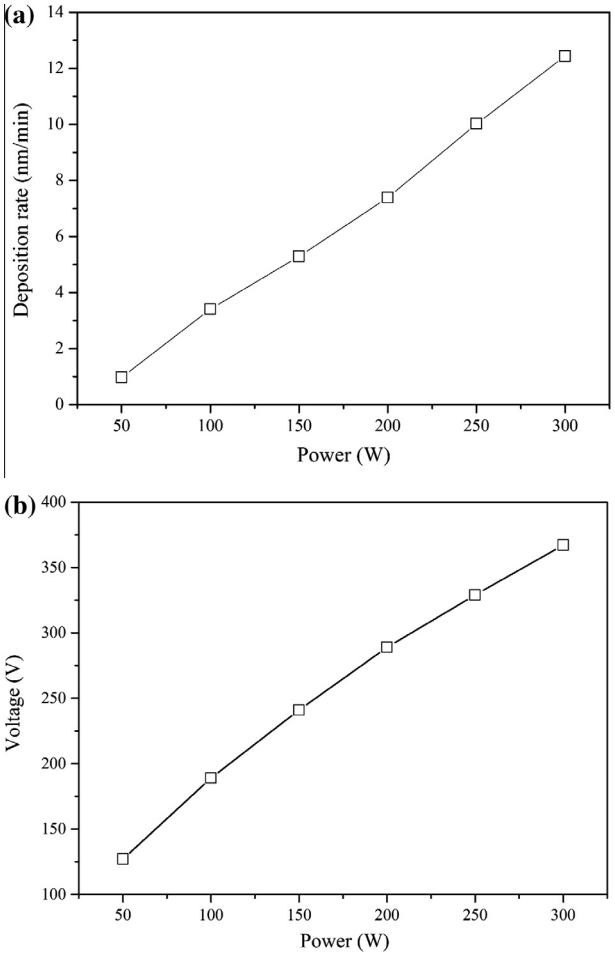

Fig. 1. (a) Deposition rate and (b) target voltage of (TiZrHf)N coatings deposited at various discharge power.

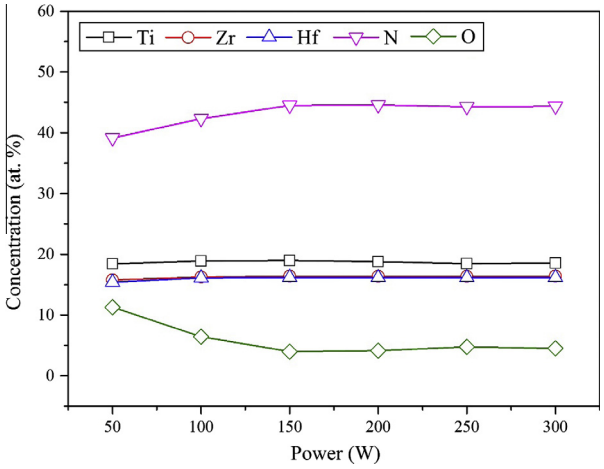

Fig. 2. Chemical compositions in (TiZrHf)N coatings deposited at various discharge power.

suggests that a balance of aforementioned factors was achieved. In this study, oxygen contamination was expected to affect the coating quality.

3.2. Crystal structure

Fig. 3 presents the XRD patterns of the (TiZrHf)N coatings deposited at various discharge powers. All of the coatings exhibited a single NaCl-type (B1) face-centered cubic (fcc) structure. The high mutual solid solubility could be explained with their same crystal structure in the individual nitrides (TiN, ZrN, HfN: fcc). The preferred orientation of the films was quantified by evaluating the integrated intensities of the three peaks present at the (111), (200), and (220) planes. The intensity of the preferred orientation is defined by the texture coefficient, $P(hkl)$ [12]:

$$P(hkl) = I(hkl)/[(111) + (200) + (220)] \quad (3)$$

where $I(hkl)$ is the measured peak integrated intensity of the (hkl) [(hkl) = (111), (200), or (220)] plane. As the discharge power increased, the preferred orientation of the (TiZrHf)N coatings changed from (2 0 0) to (1 1 1), as shown in Fig. 4. Coatings that were deposited at low discharge powers preferred the (200) plane, whereas those deposited at high discharge powers preferred the (111) plane. For nitride coatings prepared via physical vapor deposition, the (111) plane is the most commonly observed growth orientation; however, the preferred orientation changes with growth conditions. Meng et al. [13] observed a change from (200) to (111) with increasing the bias voltage in the sputtering process. Tsai et al. [14] reported that increasing the N_2 partial pressure results in a change from (111) to (200) plane. Martinez et al. [15] found a trend of the change from (200) to (111) with increasing the coating thickness. There is still no reliable explanation for the change of preferred orientation with the variation of any specific deposition parameter. Such scattered results are due partly to the complex nature of the deposition process itself and partly to the possible differences existing between deposition facilities. However, several investigators have presented the growth mechanism of transition metal nitride coatings prepared via non-equilibrium growth process. These mechanisms have been established using thermodynamic calculations. According to the thermodynamic aspect, the preferred orientation is determined based on the minimization of total energy, which is the sum of surface and strain energies. For a B1 NaCl structure, its lowest surface and strain energy planes are (200) and (111), respectively [16]. Accordingly,

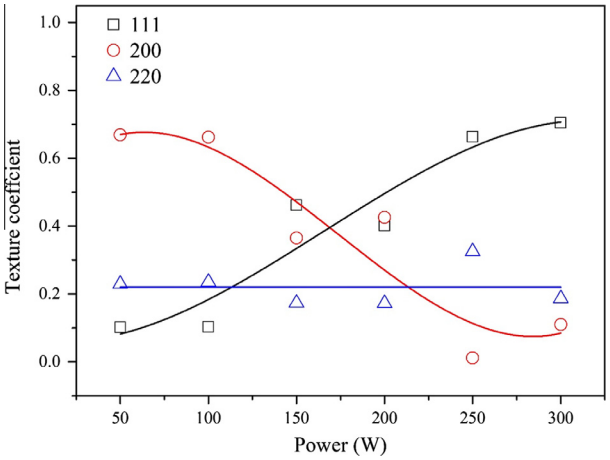

Fig. 4. Texture coefficient of the (TiZrHf)N coatings deposited at various discharge power.

the (002) preferred orientation is predicted in the deposition conditions in which the strain energy is small and the surface energy is dominant. On the other hand, the (111) preferred orientation is predicted in the deposition conditions in which the strain energy was large and dominant. Strain energy could be induced by grown-in stress that exists in a coating (i.e., intrinsic stress). Fig. 5 shows the residual stress of the (TiZrHf)N coatings as a function of discharge power. The residual stress in coatings transformed from tensile (+1.32 GPa) to compressive (−2.34 GPa) with increasing discharge power. It has been known that final residual stress of the coating is contributed by thermal stress and intrinsic stress. Difference in the coefficient of thermal expansion (CTE) between coatings and substrates produces thermal stress. This kind of stress was calculated using Eq. (4) [17]:

$$\sigma_{th} = \Delta\alpha \cdot \Delta T \frac{E_f}{(1 - \upsilon_f)} \quad (4)$$

where $\Delta\alpha$ is the difference in the CTE between the substrate and the coating, ΔT is the temperature difference between the deposition temperature and room temperature, and E_f and υ_f are the elastic modulus and Poisson's ratio of the coating, respectively. The CTE of the coatings used in the study was calculated using the rule of mixtures of the individual binary nitrides: $\alpha_{TiN} = 8.1 \times 10^{-6}\ K^{-1}$,

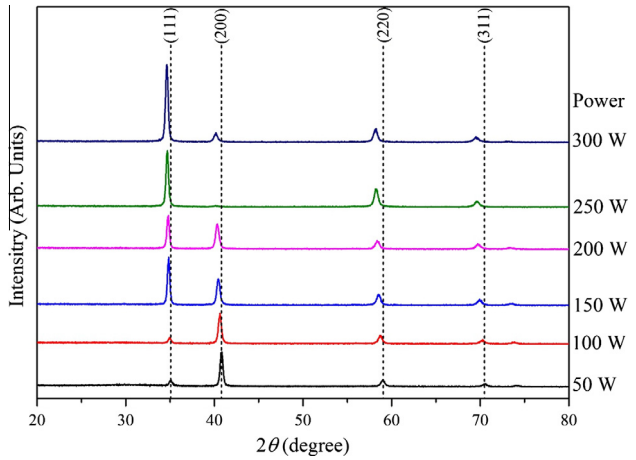

Fig. 3. X-ray diffraction patterns of the (TiZrHf)N coatings deposited at various discharge power.

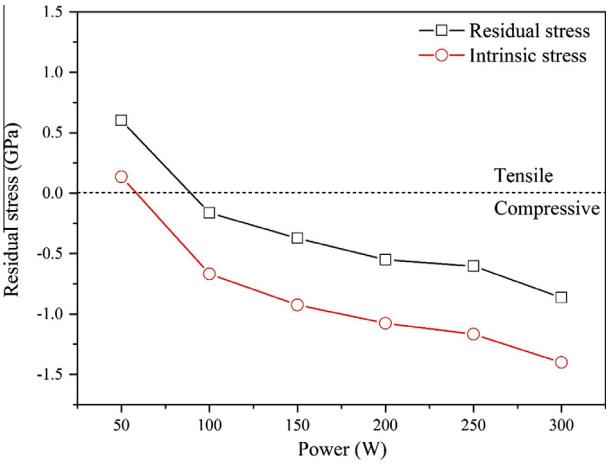

Fig. 5. The residual stress of (TiZrHf)N coatings deposited at various discharge power.

$\alpha_{ZrN} = 7.0 \times 10^{-6}\,K^{-1}$, $\alpha_{HfN} = 6.5 \times 10^{-6}\,K^{-1}$, along with the EPMA-determined composition. The Poisson's ratio of these coatings was assumed to be 0.25, which is the typical value for ceramic materials. The elastic modulus of the coatings is shown in Fig. 12a. The thermal stress was assumed as tensile in the range between 0.48 and 0.58 GPa. The intrinsic residual stress was related to the incident energetic particles that were present on the growing coating surfaces during deposition. Adatoms on the coating collided with incident ions, and these atoms were imbedded in the coating subsurface by knock-on processes, which are known to produce an atomic peening effect [18]. These "misfitted" atoms expanded the inter-planar spacing, thus creating a strain field in the surrounding matrix and increasing the lattice parameter and strain energy. In the present study, linear lattice expansion was observed with increasing discharge power (Fig. 6). Accordingly, the increased atomic peening effect at high discharge power resulted to increased strain energy. This finding led to a preference of the (1 1 1) orientation. This result agreed well with the XRD results obtained.

From the full width at half maximum intensity, the average grain sizes of the coatings were calculated using the Scherrer formula [19]. The results are shown in Fig. 6. The calculated grain sizes ranged from 22.7 nm to 25.4 nm, which was independent of discharge power. In general, the kinetic energy of adatoms was high at high discharge power; thus, the atoms moved actively on the film surface. However, in this study, depositions were performed at a high substrate temperature of 673 K. By comparison, the effect of discharge power on adatom mobility became negligible. A roughly crystalline variation of the coating was observed in the XRD results obtained. SEM and TEM were employed to investigate variations in the coating quality as a function of different discharge powers.

3.3. Microstructure

Fig. 7 shows the SEM micrographs of the (TiZrHf)N coatings deposited at different discharge powers. At low discharge powers (50 and 100 W), the structure of the (TiZrHf)ON coatings exhibited two distinct layers separated by a boundary. The underlayer has a smooth morphology without any special feature, whereas the upper layer had a columnar structure. At high discharge powers (150 W or higher), the (TiZrHf)N coatings revealed a columnar structure. The surface roughness derived by AFM revealed nearly the same value, ranging from 2.0 nm to 2.4 nm (not shown). Fig. 8 shows the TEM micrographs with selected area diffraction (SAD) patterns of (TiZrHf)ON deposited at a discharge power of 50 W. An amorphous structure was produced in the initial sputtering period (zone A); however, a columnar structure with an fcc (2 0 0)-preferred orientation, which was normal to the substrate surface, was formed as deposition time increased (zone B). Moreover, the void boundaries between the columns were clearly observed. Based on SEM observations, it is evident that the thickness of the amorphous layer decreased and eventually disappeared with increased discharge power. Fig. 9 shows the structure of (TiZrHf)N deposited at a discharge power of 250 W. The amorphous portion of (TiZrHf)N was replaced by a columnar structure. Moreover, the preferred orientation normal to substrate surface was changed to (1 1 1) and its structure became dense. To further understand the formation of the amorphous layer at lower discharge power, SIMS depth profiles was used to observe the distribution of elements and contaminations along the coating thickness, as shown in Fig. 10. The amorphous layer of the coating deposited at a discharge power of 50 W was observed to contain higher O_2 contaminations than the crystal layer. The results show that the formation of amorphous layer correlates with the amount of O_2. Meanwhile, the coating deposited at a discharge power of 250 W was observed to contain constant amounts of all of the metal elements. This finding indicates the homogeneity of the coating throughout the layer thickness (Fig. 10b).

Fig. 11 presents a schematic that summarizes the growth of (TiZrHf)N coatings as a function of discharge power. When depositions were performed at high temperatures, thermally-induced adatom mobility increased and high crystalline was formed. However, at low discharge powers, the deposited species provided weak bombardment on growing coating during sputtering. Therefore, a columnar structure separated by voids developed, mainly caused by self-shadowing. Moreover, a low deposited rate caused high levels of O_2 concentration in the initial sputtering period; consequently, amorphization of the crystalline phase was triggered [20]. As the discharge power increased, the enhanced energetic discharge species suppressed the self-shadowing, leading to the formation of a more dense structure. In addition, the amorphous layer become thinner and even disappeared, which was attributed to the reduction of oxygen concentration at high deposition rates.

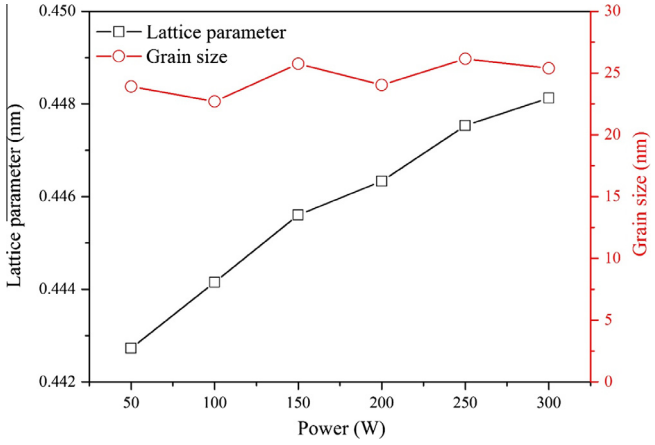

Fig. 6. Lattice parameter and average grain size of the (TiZrHf)N coatings deposited at various discharge power.

3.4. Properties

Figs. 12–14 show the mechanical properties, electrical resistivity, and light reflectivity of the (TiZrHf)N coatings as a function of discharge power. Increasing the discharge power produced denser and pure coatings; thus, the coating properties accordingly improved. As shown in Fig. 12a, the hardness of coatings initially increased from 22.7 GPa to 31.3 GPa when discharge power increased to 150 W. Nearly constant values ranging from 31.1 GPa to 32.1 GPa were obtained at discharge powers varying from 150 W to 300 W. Coating hardness was affected by several factors, including grain size, crystallographic orientations, densification of coating, residual stress, and coating composition. Previous studies [21] showed that (1 1 1) is the hardest orientation in TiN coatings due to geometrical strengthening. In this condition, hardness was expected to increase with the increase in the extent of (1 1 1)-preferred orientation. However, comparing the hardness values obtained with that in Fig. 4, the (TiZrHf)N coatings exhibited hardness values that were not consistent with that of the (1 1 1) texture coefficient. The dislocation slip, which is inactive in nanocrystalline coatings, caused texture strengthening to be ineffective on the hardness of the coating. Residual stress and grain size were considered minor factors because they exhibited small variations with discharge power. Composition variation and densification were the dominant contributions in view of the reduced oxygen contamination and elimination of visible voids with increasing

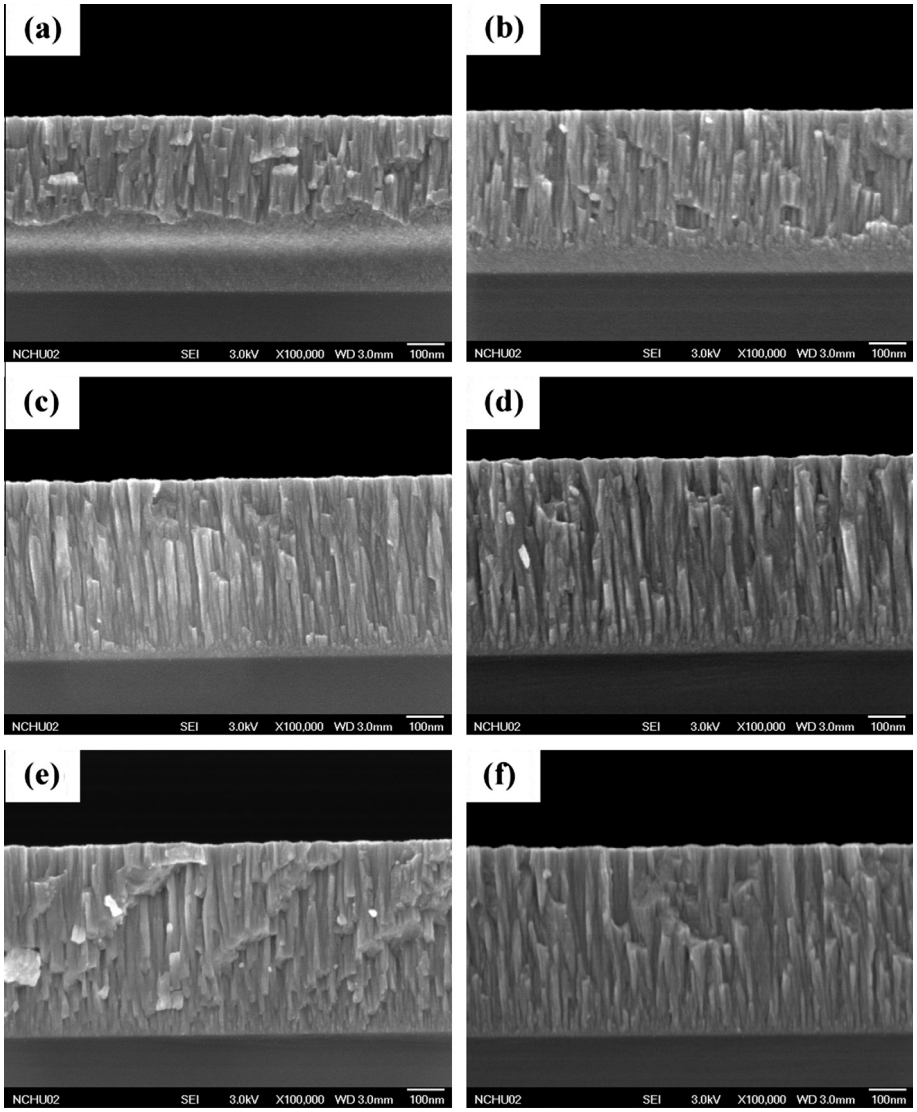

Fig. 7. SEM micrographs of the (TiZrHf)N coatings deposited at various discharge power: (a) 50 W, (b) 100 W, (c) 150 W, (d) 200 W, (e) 250 W, and (f) 300 W.

discharge power. The overall hardness of the coating was calculated using Eq. (5):

$$H_{total} = H_i - \Delta H_v + \Delta H_s + \Delta H_g \quad (5)$$

where H_i is the intrinsic hardness without stress hardening (ΔH_s), void softening (ΔH_v), and grain size strengthening (ΔH_g). The intrinsic hardness of the (TiZrHf)N coatings deposited at a discharge power of 250 W was calculated from the bulk binary nitride hardness according to the mixture rule and the EPMA-determined composition. The obtained hardness value of the coating was 16.9 GPa. Stress hardening from compressive stress was estimated after multiplying the hardness value with a correction factor. The correction factor on compressive stress used was 1.0 for simplicity. At a discharge power of greater than 150 W, void softening was ignored because voids along the boundaries occupied a small volume fraction. Grain size strengthening at different discharge powers was comparable because of similar grain size exhibited at various discharge powers. Thus, using Eq. (5), grain size strengthening was calculated to be around 14.6 GPa. Fig. 12b shows the elastic modulus as a function of hardness. Young's modulus was normally unaffected by the microstructure of the materials. However, in the present study, the elastic modulus of the films exhibited the same trend as hardness. This finding was due to an intense pressure experienced by the material in the indenter during the hardness and Young's modulus measurements. At a fixed applied load, a higher material hardness caused smaller projected area of the remaining indentation and higher average pressure in the indenter. Therefore, high hardness resulted in high values of the measured elastic modulus [22]. Moreover, the elimination of voids also enhanced the elastic modulus.

A protective coating not only requires high hardness, but also high resistance to plastic deformation during contact events. The ratio, H^3/E^2 has been increasingly applied to evaluate the resistance to plastic deformation from the values of H and E [23]. The increased value of H^3/E^2, gives information on the resistance of the material to plastic deformation. The likelihood of plastic deformation is therefore significantly reduced in materials with high H and low E. Fig. 12c shows the H^3/E^2 ratios for the (TiZrHf)N coatings as a function of discharge power. The coatings exhibited increased resistance (from 0.32 to 0.62) to plastic deformation when the discharge power was 150 W. Constant values that ranged from 0.62 GPa to 0.64 GPa were obtained when the discharge powers were between 150 and 300 W. The results obtained were consistent with the observed trend in the hardness. The present coating without substrate bias exhibited good mechanical performance; thus, this coating can be used as a protective coating.

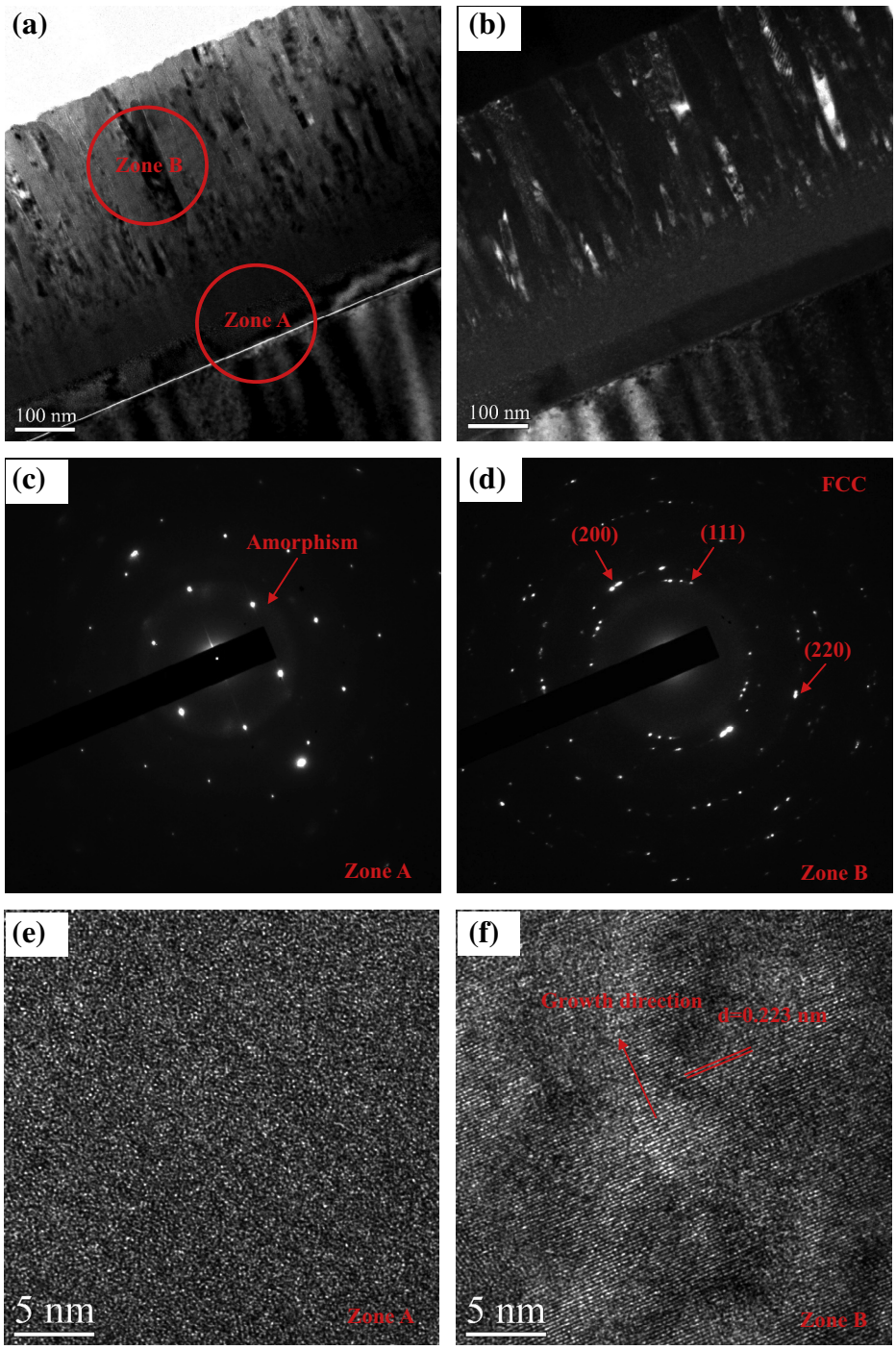

Fig. 8. Cross-sectional TEM micrographs of the (TiZrHf)N coatings deposited at discharge power is 50 W. (a) Bright-field image. (b) Dark-field image using the (1 1 1) and (2 0 0) diffraction rings indicated by circles in the SAD pattern in (d). (c) SAD pattern of zone A. (d) SAD pattern of zone B. (e) High resolution TEM lattice image of zone A. (f) High resolution TEM lattice image of zone B.

Furthermore, as shown in Fig. 13, increasing the discharge power to 200 W decreased the electrical resistivity of the (TiZrHf)N coatings from 12,424 μΩ cm to 133.5 μΩ cm until a constant value ranging from 133.5 μΩ cm to 152.3 μΩ cm was obtained. Similar to the mechanical properties, the electrical performance was dominated by composition variation and densification. In the former, the presence of oxygen atoms that are bound to the metal atoms indicates that the conduction electrons in the metal 4*d* states, which are connected to the O 2*p* states, are consumed; this phenomenon reduces the free electron density. As a result, the low O_2 contamination provides more mobile electrons; thus, electrical resistivity decreases [24]. In the latter, the decrease in voids also decreases the electrical resistivity of the coatings because the void regions possess extremely high electrical resistivity; this occurrence results in severe electron scattering [25]. The low electrical resistivity at high discharge powers contributed to the diffusion barrier in Cu metallization.

The light reflectivity of the (TiZrHf)N coating at wavelengths varying from 300 nm to 2400 nm was measured at room temperature (Fig. 14). The reflectivity spectrum exhibited a reflectivity

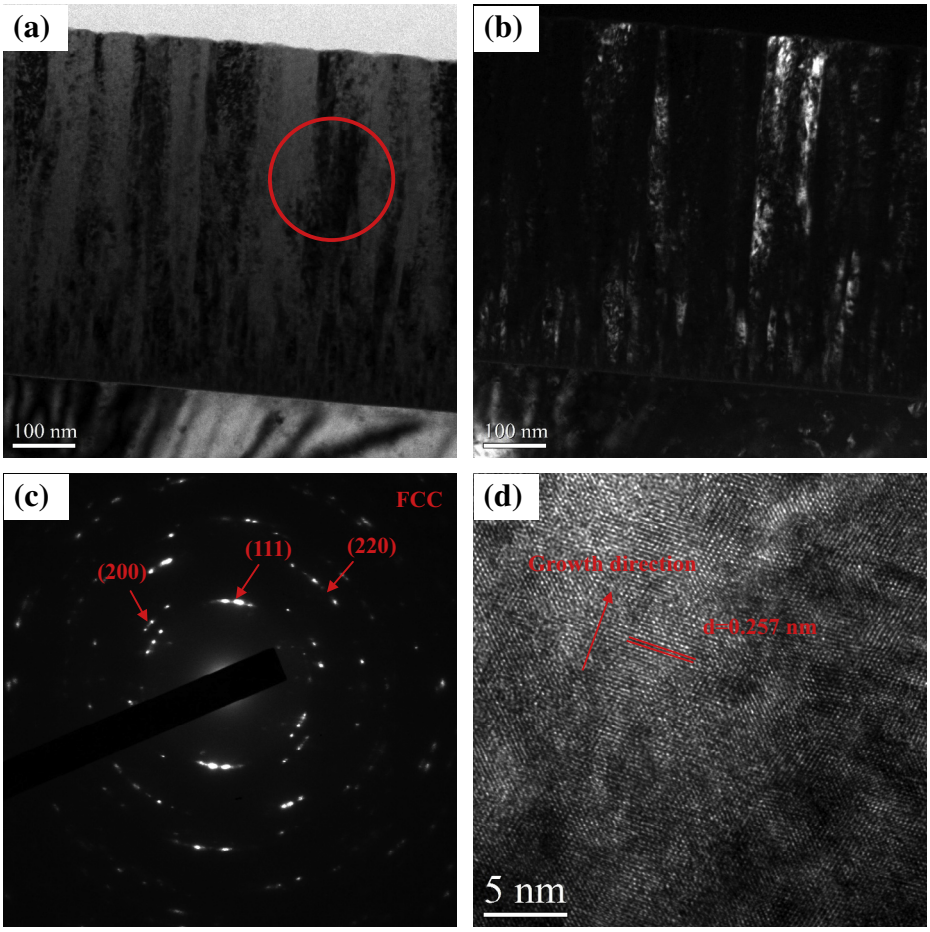

Fig. 9. Cross-sectional TEM micrographs of the (TiZrHf)N coatings deposited at discharge power is 250 W. (a) Bright-field image. (b) Dark-field image using the (1 1 1) and (2 0 0) diffraction rings indicated by circles in the SAD pattern in (c). (c) SAD pattern by circles. (e) High resolution TEM lattice image.

minimum. As the wavelength increased, the reflectivity exhibited a sharp increase and then reached a higher reflectivity, which is typical for metallic behavior. According to the Drude model [26], a changing magnetic field induces a perpendicular electric field when an electromagnetic wave traverses semi-metal films. A reflection of electromagnetic radiation then occurs. For low photon energies, the major contribution comes from intraband transitions because of free electrons. The reflectivity minimum may be associated with a collective mode of conduction electrons. For photon energies greater than that of the reflectivity minimum, interband transitions starts to predominate. The reflectivity spectra of the (TiZrHf)N coatings were characterized by a reflectivity minimum and a magnitude of reflectivity in the infrared region. The reflectivity minimum of the (TiZrHf)ON coating deposited at a discharge power of 50 W that was initially located at 2.37 eV shifted to 3.25 eV for the (TiZrHf)N coating deposited at a discharge power of 150 W. An increase in the magnitude of reflectivity in the infrared region (700–2400 nm) from 52% to 75% was observed when the discharge power increased from 50 W to 150 W. A closer examination of the reflectivity spectra revealed that the blue shift in reflectivity minimum and the change in the magnitude of reflectivity in the infrared region were negligible for discharge powers over 150 W. Even if a detailed discussion of the optical parameters of (TiZrHf)N coatings was not presented, these features were strongly affected by the chemical composition and the densification of the structure. The high reflectivity obtained (75%) in the infrared region indicates that the (TiZrHf)N coating exhibited good low-emission function, which is suitable in energy-saving coatings.

Figs. 15a and b show the representative spectra of the real part $\varepsilon_1(\omega)$ and imaginary part $\varepsilon_2(\omega)$, respectively, of the dielectric function of the (TiZrHf)N coatings deposited at different discharge powers. The spectrum was dominated by the highly polarizable free-charge carriers. This characteristic caused increasing ε_1 and decreasing ε_2 with increasing photon energy. Apart from the (TiZrHf)ON coating deposited at a discharge power of 50 W, the magnitude of ε_1 exhibited a strong free electron-like behavior that increased from a large negative value to a maximum positive value. The intersection at 0 with a positive slope indicates a longitudinal excitation mode, specifically, a screened-plasmon mode. ε_2 decreased with increased energy from a large value to a minimum at an energy greater than the screened-plasma energy. This result indicates that below this energy, a strong intraband absorption occurred. The screened plasma energy had contributions from both free and bound electrons and signaled the onset of interband transitions in the electronic structure. It can therefore be inferred that beyond the plasma energy, strong interband transitions dominated Fig. 15c shows the variations of screened-plasma energy and discharge power. The screened-plasma energy value of the (TiZrHf)N coatings shifted to higher energies from 1.396 eV to 2.515 eV when the discharge power was increased. The plasma energy is directly related to the concentration of free electrons and is defined by the following equation:

$$\omega = \sqrt{\frac{4\pi n e^2}{m^* \varepsilon_\infty}} \tag{6}$$

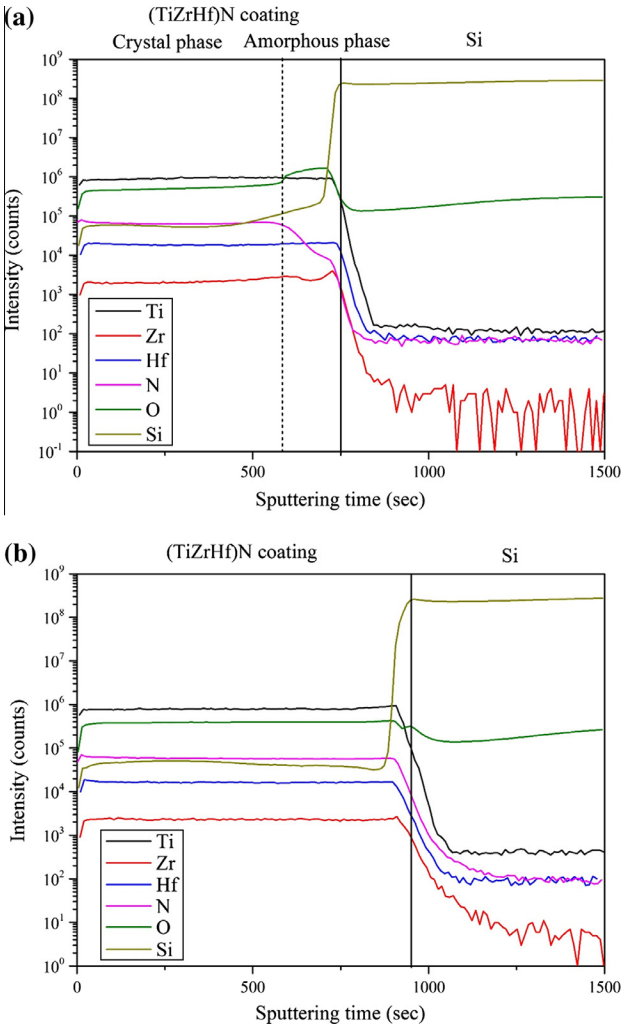

Fig. 10. The SIMS depth profiles of the (TiZrHf)N coatings deposited at various discharge power: (a) 50 W and (b) 250 W.

where n is the free electron (carrier) density, e is the electron charge, m^* is the electron effective mass, and ε_∞ is the core dielectric constant used to approximate the higher frequency electronic polarizability. Therefore, an increase in plasma energy was due to an increase in the concentration of conduction electrons. This increase was caused by increased discharge power because of low O_2 contamination. Delin et al. [27] reported that the reflectivity minimum of transition metal nitrides (e.g., TiN and ZrN) depends on screened-plasma energy. In the present study, the reflectivity minimum of the (TiZrHf)N coating was highly correlated with the screened plasma energy, as shown in Fig. 15d. Moreover, the reflectivity increased with increased discharge power. This phenomenon

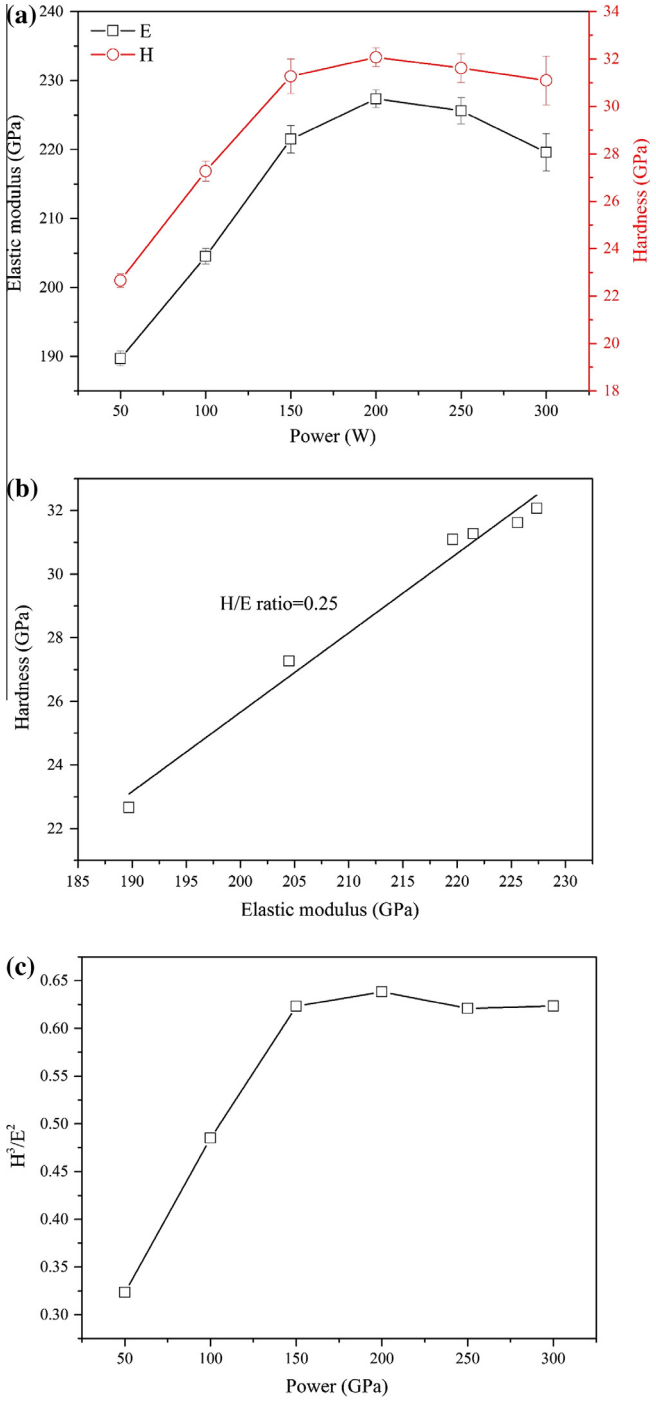

Fig. 12. (a) Hardness and elastic modulus of the (TiZrHf)N coatings deposited at various discharge power. (b) Elastic modulus of the (TiZrHf)N coatings as a function of hardness of the coatings. (c) The H^3/E^2 ratios for the (TiZrHf)N coatings as a function of discharge power.

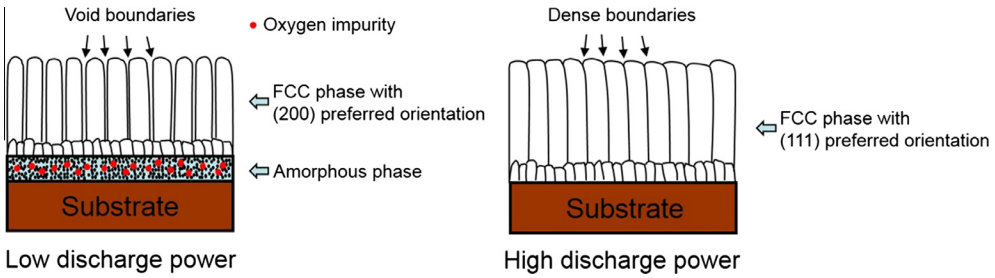

Fig. 11. Schematic diagram summarizing the growth of the (TiZrHf)N coatings.

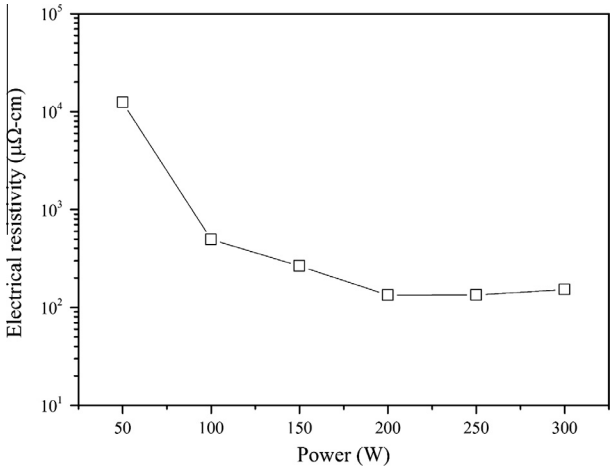

Fig. 13. Electrical resistivity of the (TiZrHf)N coatings deposited at various discharge power.

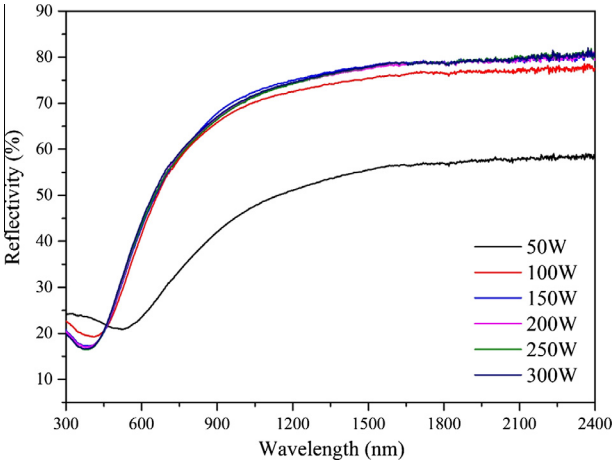

Fig. 14. Reflectivity spectra of the (TiZrHf)N coatings deposited at various discharge power.

was also attributed to the increase of conduction electrons in the coatings associated with increased discharge power [26].

Fig. 16a shows the energy loss function spectra. The energy loss function was evaluated using Eq. (7):

$$-\mathrm{Im}\left(\frac{1}{\varepsilon}\right) = \frac{\varepsilon_2}{\varepsilon_1^2 + \varepsilon_2^2} \tag{7}$$

This property involves one electron excitation and several body resonances, such as excitons or plasmons [28]. The collective behavior of electrons can be evaluated from the energy loss spectrum, where ε_2 drops to a minimum while ε_1 passes through zero. All of the spectra exhibited a strong resonance peak at approximately $\varepsilon_1 = 0$. Fig. 16b shows the variations in the resonance peak position and the loss value of the (TiZrHf)N coatings deposited at

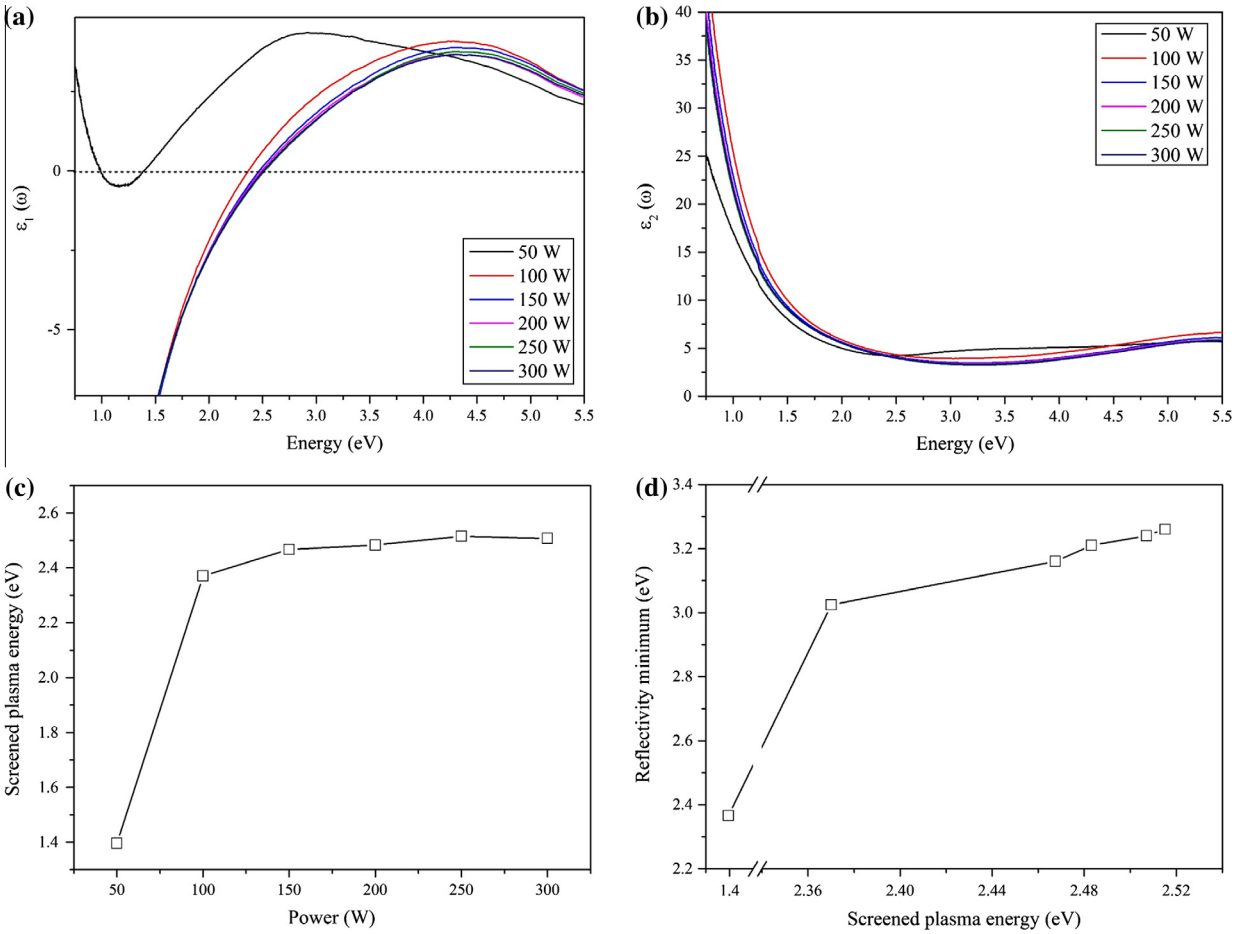

Fig. 15. Variation of (a) Real and (b) imaginary part of complex dielectric function of the (TiZrHf)N coatings deposited at various discharge power. (c) Variation of screened plasma energy as a function of discharge power. (d) Dependence of the reflectivity minimum on screened plasma energy.

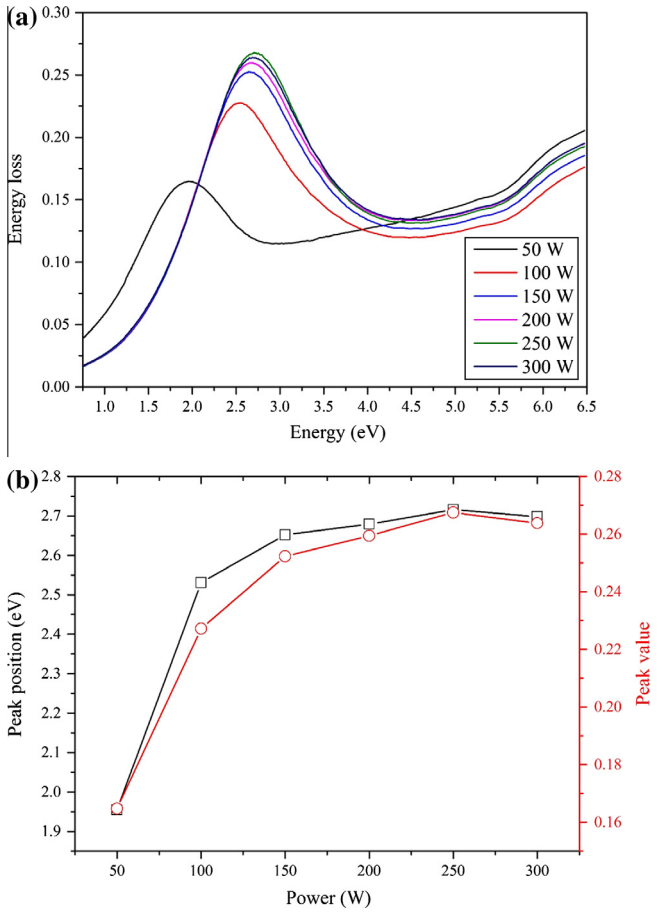

Fig. 16. (a) Energy loss function spectra of the (TiZrHf)N coatings deposited at various discharge power. (b) Variation of plasmon resonance peak position and loss value of the (TiZrHf)N coatings as a function of discharge power.

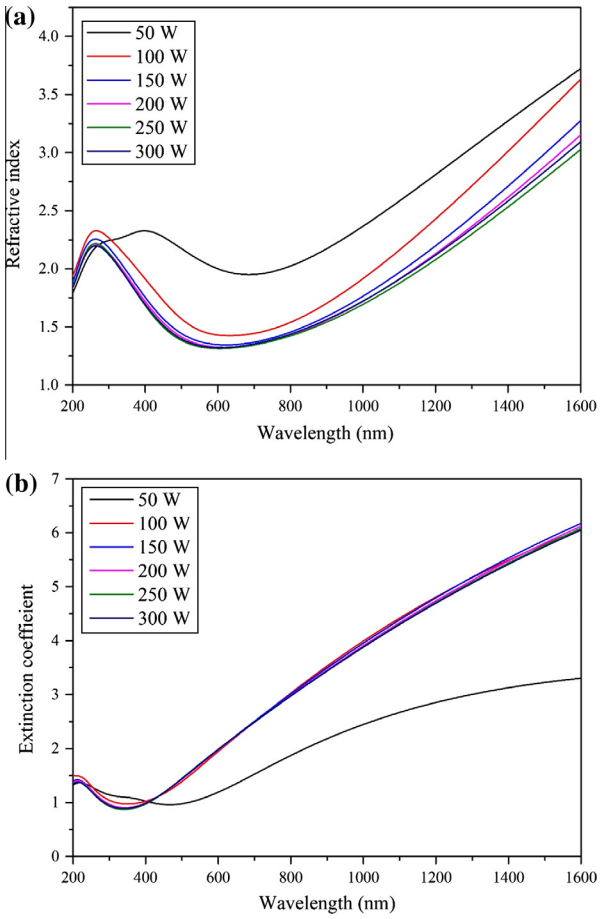

Fig. 17. Variation of (a) refractive index and (b) extinction coefficient of the (TiZrHf)N coatings deposited at various discharge power.

different discharge powers. The resonance peak blueshifted toward higher energy values from 1.96 eV to 2.70 eV because of the increase in conduction electrons. This phenomenon was responsible for the plasma reflectivity edge and corresponding characteristic color. The golden color exhibited by the coatings at a discharge power above 100 W was similar to that obtained in a previous study [29]. An increase in peak value was observed with increased discharge power. The high intensity of the energy loss maximum indicates a small amount of conduction electron damping, which is relative to electron mobility. This behavior was attributed to the decreased impurity and void density at high discharge power.

Figs. 17a and b show the calculated dependence of refractive index and extinction coefficient, respectively, of the (TiZrHf)N coatings deposited at different discharge power on photon energy. Increasing the photon energy caused the refractive index and extinction coefficient to decrease considerably, which then increased and later decreased. The extremely high values of the refractive index and extinction coefficient at low energy were associated with intraband transitions caused by free electrons. The broad peak obtained at high energy was related to interband transitions. These results provided important information to be used for optoelectronic device design using this material system.

The average specular color of the (TiZrHf)N coatings deposited at different discharge powers was represented in the CIELab color space [30], as shown in Fig. 18a. The colors for which a human eye was revealed in Fig. 18b. This graph shows that the coating deposited at a discharge power of 50 W was dark silver, which is expected at a low and negligible change in reflectivity in the visible light region. The dark silver was converted to golden-like color at a discharge power of 100 W. Reflectivity was high at the low-energy end of the visible region (red color with 700 nm wavelength and 1.77 eV energy). Reflectivity then decreased and reached extremely low values in the high-energy end of the visible region (violet color with 400 nm wavelength and 3.1 eV energy). The result of color measurement indicates higher yellowness than greenness/redness because the additive mixture of red and green reflected lights produced yellow light. This characteristic was also caused by a small destructive mixture of yellow with blue that decreased the appearance of yellowness. Thus, the coating appeared golden-like in color. Moreover, the overall reflectivity increased, which then intensified the lightness of the color. Further increase in the discharge power resulted in a brighter golden color because of increased reflectivity. The (TiZrHf)N coating may be used in decorative coatings because of its golden-like color.

4. Conclusion

In this study, (TiZrHf)N coatings were synthesized via reactive magnetron sputtering of a pure equimolar TiZrHf target on Si(100) wafers. Discharge powers ranging from 50 W to 300 W were employed. High levels of O_2 contamination occurred at low discharge power because of extremely low deposition rates. The deposited coatings exhibited a (200)-axis orientation and columnar structure. The structure contained significant void fractions between the columns and a thick amorphous underlayer. The amorphous layer exhibited decreased thickness with increased

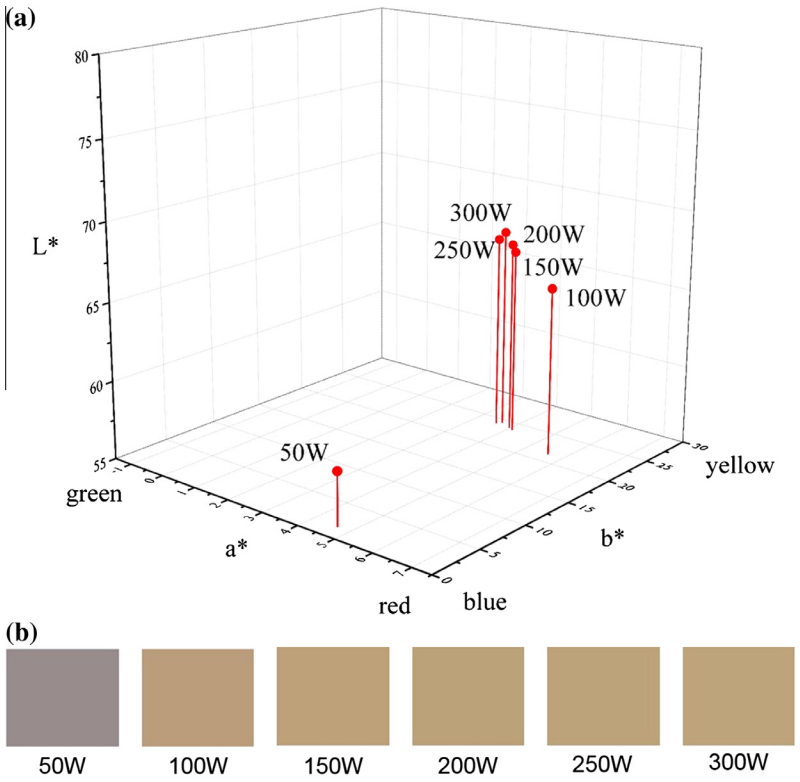

Fig. 18. (a) Average specular colors in the CIELab 1976 color space and (b) colors for a human eye of the (TiZrHf)N coatings deposited at various discharge power. (For interpretation of the references to color in this figure legend, the reader is referred to the web version of this article.)

discharge power because of reduced O_2 contamination. The coatings deposited at a high discharge power exhibited atomic peening effect; correspondingly, the compressive stress was enhanced and the preferred orientation changed from (200) to (111). Consequently, the film quality of the (TiZrHf)N coating was improved, visible voids were eliminated, and the thickness of the amorphous layer was decreased. The physical properties of the coating affected by discharge power were correlated with the O_2 contamination and voids. For coatings deposited at high discharge powers, the hardness of the coating was enhanced to approximately 32.1 GPa. Similarly, the light reflectivity in the infrared region increased to 75% and the electrical resistivity decreased to 134–152 μΩ cm. These superior physical properties indicate that the (TiZrHf)N coating can be used in various applications, such as hard coating, diffusion barrier in Cu metallization, energy-saving coating, and decorative coating.

Acknowledgments

The authors gratefully acknowledge the financial support for this research by the Ministry of Science and Technology of Taiwan under Grant No. NSC103-2221-E-005-020-MY3. The present work was also supported in part by the Center for Micro/Nano Science and Technology of the National Cheng Kung University.

References

[1] H.O. Pierson, Handbook of Refractory Carbides and Nitrides, Noyes, New Jersey, 1996.
[2] G.A. Cheng, D.Y. Han, C.L. Liang, X.L. Wu, R.T. Zheng, Influence of residual stress on mechanical properties of TiAlN thin films, Surf. Coat. Technol. 228 (2013) S328–S330.
[3] A. Kameneva, V. Karmanov, Physical and mechanical properties of the $Ti_xZr_{1-x}N$ thin films, J. Alloys Comp. 546 (2013) 20–27.
[4] Y. Kim, G. Kim, S. Lee, Influence of the N_2 partial pressure on the characteristics of CrZrN coatings synthesized using a segment CrZr target, J. Nanosci. Nanotechnol. 11 (2011) 8792–8797.
[5] Y.X. Xu, L. Chen, B. Yang, Y.B. Peng, Y. Du, J.C. Feng, F. Pei, Effect of CrN addition on the structure, mechanical and thermal properties of Ti–Al–N coating, Surf. Coat. Technol. 235 (2013) 506–512.
[6] T.D. Nguyen, Y.J. Kim, J.G. Han, D.B. Lee, Oxidation of TiZrAlN nanocomposite thin films in air at temperatures between 500 and 7000 °C, Thin Solid Films 517 (2009) 5216–5218.
[7] C.H. Ma, J.H. Huang, Haydn Chen, Residual stress measurement in textured thin film by grazing-incidence X-ray diffraction, Thin Solid Films 418 (2002) 73–78.
[8] S.A. Campbell, The Science and Engineering of Microelectronic Fabrication, Oxford University Press, New York, 2001.
[9] J.E. Mahan, Physical Vapor Deposition of Thin Films, Wiley Interscience, New York, 2000.
[10] .U. kroll, J. Meier, H. Keppner, A. Shah, S.D. Littlewood, I.E. kelly, P. Giannoulès, Origins of atmospheric contamination in amorphous silicon prepared by very high frequency (70 MHz) glow discharge, J. Vac. Sci. Technol. A 13 (1995) 2742–2746.
[11] P.K. Barhai, Neelam Kumari, I. Banerjee, S.K. Pabi, S.K. Mahapatra, Study of the effect of plasma current density on the formation of titanium nitride and titanium oxynitride thin films prepared by reactive DC magnetron sputtering, Vacuum 84 (2010) 896–901.
[12] J.H. Huang, K.W. Lau, G.P. Yu, Effect of nitrogen flow rate on structure and properties of nanocrystalline TiN thin films produced by unbalanced magnetron sputtering, Surf. Coat. Technol. 191 (2005) 17–24.
[13] Q.N. Meng, M. Wen, C.Q. Qu, C.Q. Hu, W.T. Zheng, Preferred orientation, phase transition and hardness for sputtered zirconium nitride films grown at different substrate biases, Surf. Coat. Technol. 205 (2005) 2865–2870.
[14] D.C. Tsai, Y.L. Huang, S.R. Lin, D.R. Jung, S.Y. Chang, F.S. Shieu, Structure and mechanical properties of (TiVCr)N coatings prepared by energetic bombardment sputtering with different nitrogen flow ratios, J. Alloys Comp. 509 (2011) 3141–3147.
[15] G. Martinez, V. Shutthanandan, S. Thevuthasan, J.F. Chessa, C.V. Raman, Effect of thickness on the structure, composition and properties of titanium nitride nano-coatings, Ceram. Int. 40 (2014) 5757–5764.
[16] J. Pelleg, L.Z. Zevin, S. Lungo, Reactive-sputter-deposited TiN films on glass substrates, Thin Solid Films 197 (1991) 117–128.
[17] A. Bendavid, P.J. Martin, X. Wang, M. Wittling, T.J. Kinder, Deposition and modification of titanium nitride by ion assisted arc deposition, J. Vac. Sci. Technol. A 13 (1995) 1658–1664.
[18] J.A. Thornton, D.W. Hoffman, Internal stresses in titanium, nickel, molybdenum, and tantalum films deposited by cylindrical magnetron sputtering, J. Vac. Sci. Technol. 14 (1977) 164–168.

[19] H.P. Klug, L.E. Alexander, X-Ray Diffraction Procedures for Polycrystalline and Amorphous Materials, Wiley & Sons, New York, 1974.
[20] Nguyen H. Tran, Robert N. Lamb, Lee Jene Lai, Yaw Wen Yang, Influence of oxygen on the crystalline–amorphous transition in gallium nitride films, J. Phys. Chem. B 109 (2005) 18348–18351.
[21] L. Hultman, M. Shinn, P.B. Mirkarimi, S.A. Barnett, Characterization of misfit dislocations in epitaxial (001)-oriented TiN, NbN, VN, and (Ti, Nb) N film heterostructures by transmission electron microscopy, J. Cryst. Growth 135 (1994) 309–317.
[22] S. Veprek, A.S. Argon, Towards the understanding of mechanical properties of super- and ultrahard nanocomposites, J. Vac. Sci. Technol. B 20 (2002) 650–664.
[23] T.Y. Tsui, G.M. Pharr, W.C. Oliver, et al., Nanoindentation and nanoscratching of hard carbon coatings for magnetic disks, Mater. Res. Soc. Symp. Proc. 383 (1995) 447–452.
[24] M.A. Signore, D. Valerini, A. Rizzo, L. Tapfer, L. Capodieci, A. Cappello, Investigation of the physical properties of ion assisted ZrN thin films deposited by RF magnetron sputtering, J. Phys. D: Appl. Phys. 43 (2010) 225401.
[25] D.C. Tsai, Z.C. Chang, B.H. Kuo, M.H. Shiao, S.Y. Chang, F.S. Shieu, Structural morphology and characterization of (AlCrMoTaTi)N coating deposited via magnetron sputtering, Appl. Surf. Sci. 282 (2013) 789–797.
[26] G. Frank, E. Kauer, H. Kostlin, Transparent heat-reflecting coatings based on highly doped semiconductors, Thin Solid Films 77 (1981) 107–118.
[27] A. Delin, O. Eriksson, R. Ahuja, B. Johansson, M.S.S. Brooks, T. Gasche, S. Auluck, J.M. Wills, Optical properties of the group-IVB refractory metal compounds, Phys. Rev. B 54 (1996) 1673–1681.
[28] H.R. Philipp, H. Ehrenreich, Optical properties of semiconductors, Phys. Rev. 129 (1963) 1550–1560.
[29] S. Adachi, M. Takahashi, Optical properties of TiN films deposited by direct current reactive sputtering, J. Appl. Phys. 87 (2000) 1264–1269.
[30] R.S. Hunter, R.W. Harold, The Measurement of Appearance, John Wiley and Sons, New York, 1987.